Check for updates

JGR Planets

RESEARCH ARTICLE
10.1029/2023JE008089

Measuring Erosional and Depositional Patterns Across Comet 67P's Imhotep Region

A. S. Jindal[1,2], S. P. D. Birch[2], A. G. Hayes[1], F. P. Özyurt[3], A. B. Issah[1], S. A. Moruzzi[4], M. N. Barrington[1], J. M. Soderblom[5], R. L. Kirk[6], R. Marschall[7], and J. B. Vincent[8]

[1]Cornell Center for Astrophysics and Planetary Sciences, Cornell University, Ithaca, NY, USA, [2]Department of Earth, Environmental and Planetary Sciences, Brown University, Providence, RI, USA, [3]Department of Physics, Wellesley College, Wellesley, MA, USA, [4]Lunar and Planetary Laboratory, The University of Arizona, Tucson, AZ, USA, [5]Department of Earth, Atmospheric and Planetary Sciences, Massachusetts Institute of Technology, Cambridge, MA, USA, [6]US Geological Survey, Astrogeology Science Center, Flagstaff, AZ, USA, [7]CNRS, Observatoire de la Côte d'Azur, Laboratoire J.-L. Lagrange, Nice, France, [8]Deutsches Zentrum fur Luft-und Raumfahrt (DLR), Institut für Planetenforschung, Berlin, Germany

Abstract Comet 67P/Churyumov-Gerasimenko displays a pronounced hemispherical dichotomy in surface morphology, where the southern hemisphere exhibits more erosional features than the northern hemisphere due to receiving much greater solar radiation. Consequently, it is generally assumed that particles are ejected from the southern hemisphere through sublimation and a significant fraction eventually descends as airfall, covering the northern terrains. To investigate this south-to-north material transfer during the comet's perihelion passage, we used photoclinometry to measure material redistribution within its most extensive smooth terrain deposit around the Imhotep region. However, our findings do not align with this expected trend. Instead, we show that local-scale processes substantially impact the erosion and accumulation of material, with one area experiencing net erosion while another nearby region, just a few dozen meters away, sees sediment buildup. Our analysis underscores the complex interplay of processes shaping Comet 67P's surface and likely comets more generally.

Plain Language Summary Comets are composed of some of the most primitive materials in the solar system, having spent most of their lifetimes in the far reaches of the outer solar system, shielded from the Sun's radiation. Jupiter Family Comets (JFCs) are a class of comets that get pulled into the inner solar system due to Jupiter's gravity. While JFCs still preserve abundant primordial materials, their new orbits expose them to significantly higher solar insolation, resulting in sublimation-driven surface activity. The processes driving this activity, however, need to be better constrained. Observations of comet 67P/Churyumov-Gerasimenko's (a JFC) surface indicate that particles are ejected from its southern hemisphere through sublimation, and a significant fraction eventually descends as "airfall," covering its northern terrains. To investigate this south-to-north material transfer during the comet's perihelion passage, we measured material redistribution within its largest "airfall" deposit. However, our findings do not align with this expected trend. Instead, we show that local-scale processes substantially impact the erosion and accumulation of material, with one area experiencing net erosion while another nearby region, just a few meters away, sees sediment buildup. Our analysis highlights the complex interplay of processes shaping Comet 67P's surface and likely comets more generally.

Key Points:

- We provide a method for measuring erosion and deposition values across 67P's smooth terrains with cm-scale accuracy
- While sediment mostly accumulates in the topographic lows of Imhotep, there is no clear trend indicating south-to-north transport of sediment
- Local-scale processes have significant impacts on the overall re-distribution of material

Supporting Information:

Supporting Information may be found in the online version of this article.

Correspondence to:

A. S. Jindal,
abhinav_jindal@brown.edu

Citation:

Jindal, A. S., Birch, S. P. D., Hayes, A. G., Özyurt, F. P., Issah, A. B., Moruzzi, S. A., et al. (2024). Measuring erosional and depositional patterns across Comet 67P's Imhotep region. *Journal of Geophysical Research: Planets*, *129*, e2023JE008089. https://doi.org/10.1029/2023JE008089

Received 15 SEP 2023
Accepted 8 FEB 2024

Author Contributions:

Conceptualization: A. S. Jindal, S. P. D. Birch, A. G. Hayes
Data curation: A. S. Jindal, S. P. D. Birch, M. N. Barrington
Formal analysis: A. S. Jindal, S. P. D. Birch, F. P. Özyurt, A. B. Issah
Funding acquisition: S. P. D. Birch, A. G. Hayes
Investigation: A. S. Jindal, S. P. D. Birch, A. G. Hayes, M. N. Barrington, J. M. Soderblom, R. L. Kirk, R. Marschall, J. B. Vincent
Methodology: A. S. Jindal, F. P. Özyurt, A. B. Issah, S. A. Moruzzi, R. L. Kirk
Project administration: A. G. Hayes
Resources: A. S. Jindal, S. P. D. Birch, A. G. Hayes
Supervision: A. S. Jindal, A. G. Hayes
Validation: A. S. Jindal, S. P. D. Birch, A. G. Hayes, M. N. Barrington, J. M. Soderblom, R. L. Kirk, R. Marschall, J. B. Vincent

© 2024. American Geophysical Union. All Rights Reserved.

1. Introduction

Comets are composed of some of the most primitive materials in the solar system, having spent most of their lifetimes in the far reaches of the outer solar system, shielded from the Sun's radiation. Comet 67P/Churyumov-Gerasimenko (hereafter 67P) is a Jupiter Family Comet—a class of comets that orbits closer to the Sun, often having moderately eccentric orbits that take them from just beyond Jupiter's orbit to heliocentric distances similar to Earth's (Levison & Duncan, 1997). 67P is on a 6.44-year orbit around the Sun that takes it from 1.24 AU during its perihelion passage to 5.68 AU at aphelion. This gives rise to the sublimation-driven activity on the surface, which can modify the comet's landscapes in significant ways. The current configuration of 67P's orbit is such that summer in the comet's southern hemisphere nearly coincides with its perihelion passage, and hence, the southern hemisphere receives significantly greater insolation rates than the northern hemisphere (Keller et al., 2015; X. Hu et al., 2017). This gives rise to a seasonal mass transfer system, where a large fraction of mostly cm-sized or larger particles that are liberated from southern latitudes of the nucleus during the southern summer fall back as "airfall"

Visualization: A. S. Jindal, S. P. D. Birch, A. G. Hayes
Writing – original draft: A. S. Jindal
Writing – review & editing: A. S. Jindal, S. P. D. Birch, A. G. Hayes, S. A. Moruzzi, M. N. Barrington, J. M. Soderblom, R. L. Kirk, R. Marschall, J. B. Vincent

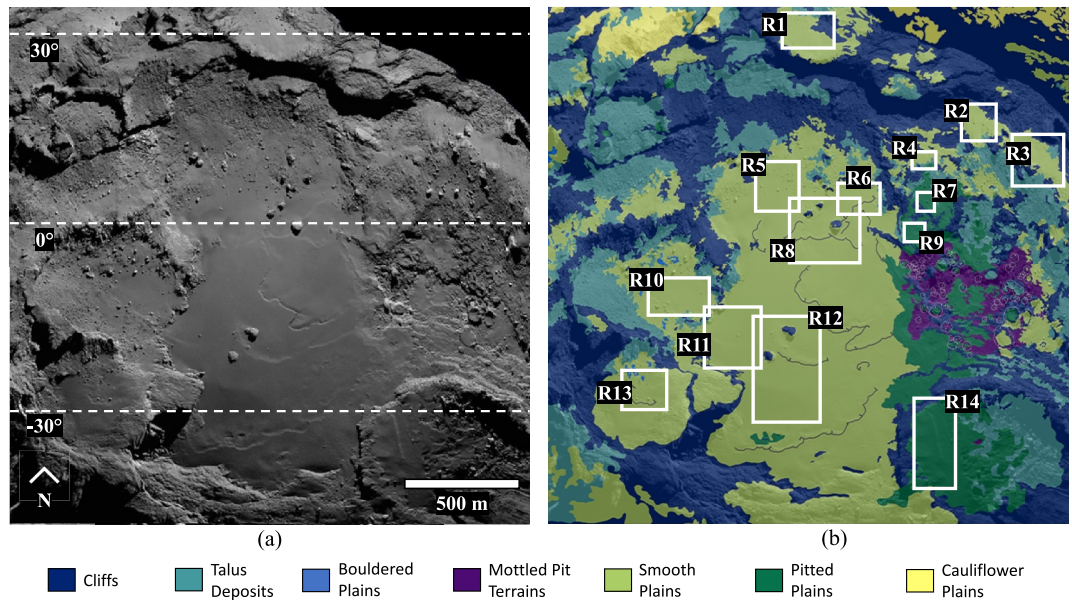

Figure 1. Overview of sub-regions where digital elevation models (DEMs) were created. (a) Equirectangular projection of the Imhotep region; the equator passes through the region, allowing us to observe sediment re-distribution in both the south and north. (b) Image from panel (a) overlayed with geomorphic units as defined by Birch et al. (2017) and boxes highlighting the regions where DEMs were created. We created 14 DEMs (R1–R14) in regions dominated by "smooth terrains" (smooth plains, pitted plains, cauliflower plains) where signs of erosion/deposition were observed.

into the colder gravitational lows of the northern hemisphere (Keller et al., 2017; N. Thomas et al., 2015). This is evidenced most clearly by a hemispheric dichotomy in 67P's global surface morphology (Birch et al., 2017; Vincent et al., 2017). Specifically, the southern hemisphere of the comet is dominated by layered bedrock units that represent the exposed nucleus ("rough" terrains), while topographically smooth deposits of mostly centimeter-to-decimeter sized particles ("smooth" terrains) cover a significant fraction of 67P's northern hemisphere (Birch et al., 2017; M. R. El-Maarry et al., 2016; Thomas et al., 2018).

The European Space Agency's Rosetta spacecraft orbited 67P throughout its perihelion passage during the peak of its activity from August 2014 through September 2016 (67P reached perihelion on 13 August 2015). The data acquired by the Rosetta mission have allowed us to resolve material transport across a cometary surface for the first time. These observations, detailed in multiple previous studies (Barrington et al., 2023; Birch et al., 2019; El-Maarry et al., 2017; Fornasier et al., 2017; O. Groussin et al., 2015; Keller et al., 2017; Jindal et al., 2022) have shown that, while sediment may broadly migrate northward through time, local processes significantly modify 67P's surface geology over timescales far shorter than a single orbit. How much of 67P's global geology is set by global, seasonally driven processes versus local (<100m scale) processes, and whether the presently observed smooth terrains are terminal deposits for sedimentary particles, therefore, remain poorly constrained.

To date, only a few studies have attempted to quantify sediment transport rates on 67P (X. Hu et al., 2017; P. Cambianica et al., 2020, 2021). Similar to previous studies, our work targets the smooth terrains of 67PS, which include the smooth plains, pitted plains, and cauliflower plain morphologies defined by Birch et al. (2017). The smooth terrains also host the most rapid changes on 67P that Rosetta observed (Barrington et al., 2023; Birch et al., 2019; El-Maarry et al., 2017; Fornasier et al., 2017; O. Groussin et al., 2015; Jindal et al., 2022), unlike the consolidated material (Pajola et al., 2017) which displayed very few changes, most of which were traced back to outbursts. Understanding the processes driving the evolution of 67P's smooth terrains is, therefore, crucial to understanding 67P's overall geological evolution.

We focus specifically on the face of the large lobe of 67P (Figure 1), encompassing the entire Imhotep region and small portions of the Ash and Khepry regions. The large lobe consists of regions of smooth terrains in both the southern and northern parts of the comet and is therefore an opportune place to look for evidence of sediment transport from the south to the north. Most of the observed surface changes in this region took place between 05/2015 and 01/2016 (Barrington et al., 2023; El-Maarry et al., 2017; O. Groussin et al., 2015; Jindal et al., 2022). To

21699100, 2024, 2, Downloaded from https://agupubs.onlinelibrary.wiley.com/doi/10.1029/2023JE008089 by Universite Cote D'azur, Wiley Online Library on [09/01/2025]. See the Terms and Conditions (https://onlinelibrary.wiley.com/terms-and-conditions) on Wiley Online Library for rules of use; OA articles are governed by the applicable Creative Commons License

measure the total change in the sediment in these regions, we employ a shape-from-shading technique to create Digital Elevation Models (DEMs) for our regions of interest (ROIs) from images obtained before and after changes are observed on the surface (Section 2). We then compare our DEMs spatially and temporally, identifying trends in the topographic evolution of the smooth terrains in the broader Imhotep region (Section 3). In tracking the re-distribution of sediment over 67P's perihelion passage over a significant portion of 67P's surface, including some of its most active regions, we provide a template that can be used across the rest of 67P to understand its sediment budget, and landscape evolution, more generally.

2. Methods

We use the Ames Stereo Pipeline's (ASP) shape-from-shading tool (Alexandrov & Beyer, 2018) to create photoclinometric DEMs in our ROIs. Shape-from-shading, or photoclinometry, is a technique that estimates surface topography by modeling the variation in the intensity of light recorded in images and has been widely utilized to generate topography for planetary surfaces (Lesage et al., 2021; Lohse et al., 2006; Tenthoff et al., 2020) including comets (X. Hu et al., 2017; Tang et al., 2019). For our study, we used images of 67P's surface obtained by Rosetta's Optical, Spectroscopic, and Infrared Remote Imaging System (OSIRIS, Keller et al. (2007)). The position of the camera and the Sun with respect to the surface of the comet when an image was acquired is obtained using image header information and routines in the Navigation and Ancillary Information Facility (NAIF) SPICE toolkit (Acton, 1996). We used the Hapke function (Hapke, 2012) to describe the photometric properties of the surface following previous studies (Fornasier et al., 2015).

2.1. Source Data

We made DEMs of smooth terrains on the large lobe of 67P where signs of erosion/deposition were observed (Figure 1). This includes regions where new boulders are exposed, or where previously observed boulders became buried under sediment. This technique requires that these ROIs are largely photometrically uniform. Accordingly, we select regions that are primarily draped with smooth terrains and contain minimal consolidated material. This minimizes errors in the shape-from-shading process, which assumes uniform photometric properties for the surface to derive slopes and thus elevation.

The OSIRIS camera system on board Rosetta consists of a Narrow Angle Camera (NAC) designed to study the comet's surface and a Wide Angle Camera designed to study the comet's near-nucleus environment (Keller et al., 2007). We use NAC images obtained using the F22 and F82 filters, which are centered at 649 nm and provide the best signal-to-noise ratio. We are interested in finding images covering our ROIs across two time periods: Period 1 (08/2014–05/2015) spans the time period prior to when the first large-scale changes were observed on the large lobe before perihelion, and Period 2 (01/2016–09/2016) covers the time period where the final changes in this region were observed, post-perihelion. For each ROI, we typically identify 3–4 images in each period to generate DEMs, allowing us to quantitatively map the net change in sediment thickness over the course of Rosetta's mission. Multiple images are selected such that they have varying solar azimuths (ideally, with differences close to $\pm 90°$) when possible, as this aid the photoclinometry algorithm to constrain slopes in multiple directions. With one exception (Table S16 in Supporting Information S1), we limit our data set to images with pixel scales better than $\sim$1 m/pixel. We also limit our study to images with low incidence angles, which avoid images with large shadows, and low emission angles, which ensure that steep slopes can be accurately interpreted by photoclinometry. Because most portions of the large lobe of the comet have particularly good image coverage within our periods of interest, numerous images typically meet these criteria.

Photoclinometry requires accurate knowledge of the viewing geometries of the input images. We obtain this by using image header information and routines in the NAIF SPICE toolkit (Acton, 1996) along with the 4 million plate SHAP4S shape-model for 67P (F. Preusker et al., 2015). The SHAP4S model is developed from data acquired before the inbound equinox and hence captures the topography of the terrains prior to the changes that took place as 67P approached the perihelion. We use this shape model to create low-resolution DEMs for our ROIs that serve as an input to photoclinometry.

2.2. Bundle Adjustment

When multiple images are used as inputs for shape-from-shading, errors in the calculated camera positions and orientations for each image can produce errors in the output DEMs, requiring an initial correction. We do so

21699100, 2024, 2, Downloaded from https://agupubs.onlinelibrary.wiley.com/doi/10.1029/2023JE008089 by Universite Cote D'azur, Wiley Online Library on [09/01/2025]. See the Terms and Conditions (https://onlinelibrary.wiley.com/terms-and-conditions) on Wiley Online Library for rules of use; OA articles are governed by the applicable Creative Commons License

21699100, 2024, 2, Downloaded from https://agupubs.onlinelibrary.wiley.com/doi/10.1029/2023JE008089 by Universite Cote D'azur, Wiley Online Library on [09/01/2025]. See the Terms and Conditions (https://onlinelibrary.wiley.com/terms-and-conditions) on Wiley Online Library for rules of use; OA articles are governed by the applicable Creative Commons License

through a bundle-adjustment approach. The ASP has its own bundle-adjustment tool (Beyer et al., 2018), which operates by finding matching tie points, computing corresponding triangulated points in 3D space, and then minimizing the pixel re-projection errors for these points using the Ceres least square solver (Agarwal & Mierle, 2012). This approach relies on having a significant overlap between the input images and a high density of selected tie points. Instead of bundle adjusting all images used in our study, we bundle adjust a subset of images that cover each of our ROIs individually. Images from both Periods 1 and 2 for a given ROI are bundle-adjusted together so that the DEM outputs for each of these periods can be directly compared to one another. This requires manual selection of tie points across the images since the terrain changes (quite significantly for some regions) between the two time periods and because the images are preferentially selected to have variable illumination. While the terrain makes the change between the two periods, these changes mostly occur within the smooth terrains, and there are static features such as boulders and cliffs that provide enough tie points. For this reason, we select ROIs that have at least a few static features interspersed within the smooth terrains. Finally, we use an initial DEM extracted from the shape model such that it covers the overlapping area between the images being bundle-adjusted as an additional constraint for the triangulated points.

This process reduces the pixel re-projection errors within our images from an initial value of order 10 pixels to a final value that is of order 1 pixel. Bundle adjustment is an essential step for multi-image shape-from-shading. If the input images are not correctly aligned, it will erroneously result in individual features repeatedly showing up in the resulting DEM. For example, when images are not properly aligned, an individual boulder may appear multiple times in the same DEM. In order to avoid such errors, we only use images that have median residual errors lower than 1.5 pixels as input for the shape-from-shading process.

2.3. Shape-From-Shading

A variety of shape-from-shading techniques have been used for over 70 years (van Diggelen, 1951) to calculate surface topography based on variations in the brightness of pixels in images, which depend both on the positions of the light source and the camera with respect to the local surface normal, and the photometric properties of the surface. In the ASP, an initial DEM is required as an input to generate a simulated image for a given ROI. This is obtained from the shape model by extracting a radius map over the ROI, and then subtracting the mean radius over this area to get a height map. The ROIs are kept small enough to ensure that the radius does not change by a large fraction across them (as occurs in some areas, given 67P's highly irregular shape). The ASP's shape-from-shading algorithm then iterates over this initial DEM, adjusting elevations until the simulated light intensity agrees well with the light intensity as observed by the camera. The 4 million plate SHAP4S models we used to generate the initial DEM has an average sampling distance of ∼4 m (F. Preusker et al., 2015). In short, the initial DEM from the shape model accurately captures the long-wavelength topography, and the DEM created through shape-from-shading captures variations in topography at the pixel scale (which is ∼0.5 m for most of our images) capturing the small-scale topographic variations we are interested in (Figure 2).

The ASP also requires prior knowledge of the surface photometric properties to generate a simulated image; in this study, we use a Hapke reflectance model (Hapke, 2012) to represent our surface. Hapke coefficients have been determined for several morphologies for both pre- and post-perihelion images of 67P using the technique described by Fornasier et al. (2015) and applying it to individual terrain types. We utilized Hapke coefficients determined for the 649 nm wavelength (F22 and F82 filters) for the smooth plains and pitted plains of 67P for pre- and post-perihelion (Tables S1 and S2 in Supporting Information S1). The outcome of photoclinometry is not sensitive to variation in the value of the Hapke parameters within their errors. Along with maximizing the agreement between the simulated image and the image as obtained by the NAC, ASP's shape-from-shading also allows the user to specify a smoothness weight (μ) and an initial DEM constraint weight (λ). We used values of $\mu = 10^{-4}$ and $\lambda = 10^{-5}$ to create our DEMs, ensuring that we do not artificially smooth the surface topography within them and that our DEMs can vary from the shape model input sufficiently. The latter of these factors is especially important for the DEMs generated for Period 2 as the topography has varied significantly from what is predicted by the shape model, itself an estimate of the surface topography before the numerous large-scale near-perihelion surface changes (Preusker, F. et al., 2015). Values of 10^{-3} and 10^{-5} were also explored for μ but resulted in the DEM being too blurry and too noisy respectively. Similarly, a higher value of $\lambda = 10^{-4}$ was explored but resulted in the retention of artifacts from the shape model used to generate the input DEM.

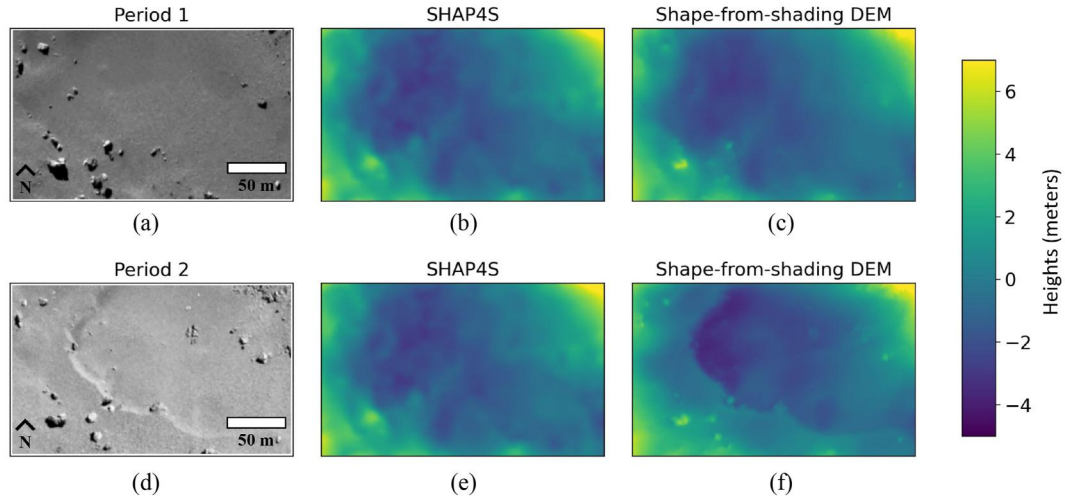

Figure 2. Comparison between heights predicted by the SHAP4S shape model and our shape-from-shading digital elevation models (DEMs). Panels (a–c) show an image, heights predicted by the shape model, and heights predicted by the DEM for Period 1 in region R10, while panels (d–f) show the same for Period 2. While the terrain appears to have changed considerably between the two periods, this is not registered in the shape model, but our DEMs capture this change very distinctly. Moreover, the shape-from-shading DEMs also capture the smaller scale topography.

We use multiple bundle-adjusted images as inputs for shape-from-shading. Though a single-image approach to photoclinometry has been used to create DEMs for 67P in the past (X. Hu et al., 2017; Tang et al., 2019), such approaches create artifacts in the form of topographic streaks in the along-sun direction. Such artifacts are worsened by variations in surface albedo but are present even where the photometric behavior is uniform. Although these streaks can be suppressed by using de-striping techniques based on spatial filtering (Kirk et al., 2003), the topography is still less accurate in the cross-sun direction. Having multiple images with a range of solar azimuths helps resolve this issue (Section 2.1). While the input images are selected to include a variety of solar azimuths and minimize shadows (low solar incidence), shadows cannot be avoided altogether. Shadowed areas can be misinterpreted as having very low light intensity, resulting in steep slope estimates facing away from the Sun that will lead to errors. To minimize this error, we use the shadow threshold parameter in ASP's shape-from-shading tool, which creates a map of the pixels in an image that lie within shadows. As a result, if one of the input images has a given area with a large fraction of pixels within shadows, the contribution of this image to calculating heights for this area will be ignored. The shadow thresholds are calculated individually for each image, and may vary across different ROIs for the same image (values can be found in Tables S3–S16 in Supporting Information S1).

2.4. Measurements and Validation

Once we have generated multiple DEMs from both periods for each ROI, we compare them to each other to directly measure the volume of sediment that was lost or gained during 67P's perihelion passage. Because all DEMs for a given ROI for both periods are built using the same geodetic datum, they can be directly compared to one another. We are mindful that the DEMs may be unreliable in sub-regions that are not dominated by smooth terrains (smooth plains and pitted plains), as the Hapke coefficients we use are representative of the scene, derived for the smooth terrains, and do not represent other surfaces such as boulders, exposed bedrock, and/or other consolidated materials. To address this, we limit our analysis to polygons drawn over our ROIs, avoiding any boulders and other patches of photometrically different terrains. The polygons are picked such that the overall change of sediment from Period 1 to 2 within the polygon is not highly variable, that is, we ensure that we do not pick a single polygon over an area that undergoes both erosion and deposition. To measure changes in elevation from sediment transport, we computed the average elevation value within these polygons and compared the averages between the two periods (Figure 3). By comparing average elevations within these polygons rather than doing a point-to-point comparison, we minimize any errors that may arise due to slight misalignment between the DEMs. The difference in the mean elevation of a polygon from Period 1 to Period 2 represents the change in

21699100, 2024, 2, Downloaded from https://agupubs.onlinelibrary.wiley.com/doi/10.1029/2023JE008089 by Universite Cote D'azur, Wiley Online Library on [09/01/2025]. See the Terms and Conditions (https://onlinelibrary.wiley.com/terms-and-conditions) on Wiley Online Library for rules of use; OA articles are governed by the applicable Creative Commons License

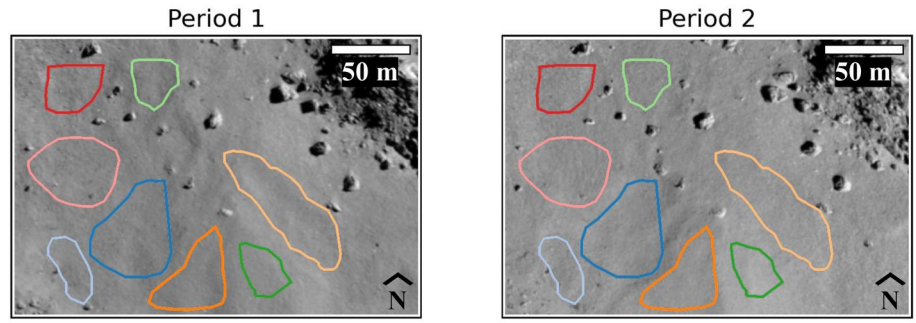

(a) (b)

Polygon	Method 1	Method 2
Polygon 1	-0.50 ± 0.02 m	-0.56 ± 0.11 m
Polygon 2	0.65 ± 0.02 m	0.53 ± 0.10 m
Polygon 3	1.29 ± 0.02 m	1.20 ± 0.14 m
Polygon 4	-0.33 ± 0.01 m	-0.17 ± 0.06 m
Polygon 5	-1.05 ± 0.03 m	-1.19 ± 0.10 m
Polygon 6	-0.15 ± 0.02 m	-0.22 ± 0.03 m
Polygon 7	1.00 ± 0.04 m	0.86 ± 0.11 m
Polygon 8	0.45 ± 0.02 m	0.54 ± 0.15 m

(c)

Figure 3. Sediment re-distribution in region R1. Panels (a, b) show Periods 1 and 2, respectively. The polygons are drawn to avoid boulders and consolidated materials and to track visible morphological changes. Panel (c) shows a comparison for the change in elevation for each polygon along with the associated errors using the two different methods described in Section 2.4, where Method 1 uses the full compilation of images and the Ames Stereo Pipeline's error tool and Method 2 is the "check" where multiple digital elevation models derived from single image pairs are used.

sediment thickness, where a negative value implies erosion, and a positive value implies the deposition of new sediment (Figures S8–S21 in Supporting Information S1).

Calculating the errors in our DEMs is a complex process as errors can arise from random errors in the image signal, uncertainties in the camera orientation and calibration, as well as from errors in our assumed photometric function. By the bundle adjusting the input images used to produce the DEMs and using Hapke coefficients derived for specific terrain types before or after the comet's near-perihelion activity, we minimize the errors from the second and third sources. To estimate the final uncertainty in our measurement of sediment change, we used ASP's built-in error estimation tool (Figure 3, Method 1). This tool computes the minimum height perturbation at each grid point of the output DEM that is required to make at least one of the input image simulations (Section 2.1) deviate by more than twice the discrepancy between the actual image and the unperturbed simulated image. As a check on ASP's tool, we also estimated the error by creating 3 DEMs for each of the two periods, using only a subset of two-image pairs from the available image set over region R1 (Figure 3, Method 2). The two-image pairs are selected such that the difference in the solar azimuths between the two images is as close to ±90° as possible. By subtracting the mean values within the sub-regions described above of each of the 3 DEMs for Period 1 from each of the 3 DEMs for Period 2, we obtain 9 measurements for the change in sediment for each sub-region. We calculate the mean and standard deviation for these 9 measurements to obtain a singular value for the change in sediment within each sub-region and the associated error (Figure 3). A comparison between the values obtained from these two methods shows that the estimated values agree well within the error (Figure 3c). It is important to note that the errors from ASP's error estimation tool (Method 1) provide an optimistic estimate of the uncertainty in the measurement of the change in elevation when compared to Method 2. However, even for Method 2, the uncertainty stays within ~0.1 m, far less in scale than any topographic feature we seek to measure. Since it is not always possible to create multiple DEMs for each period as required for Method 2, for the rest of our ROIs in our study, we present the uncertainty in sediment re-distribution as obtained from Method 1. Though more optimistic, this provides a consistent method throughout all ROIs.

21699100, 2024, 2, Downloaded from https://agupubs.onlinelibrary.wiley.com/doi/10.1029/2023JE008089 by Universite Cote D'azur, Wiley Online Library on [09/01/2025]. See the Terms and Conditions (https://onlinelibrary.wiley.com/terms-and-conditions) on Wiley Online Library for rules of use; OA articles are governed by the applicable Creative Commons License

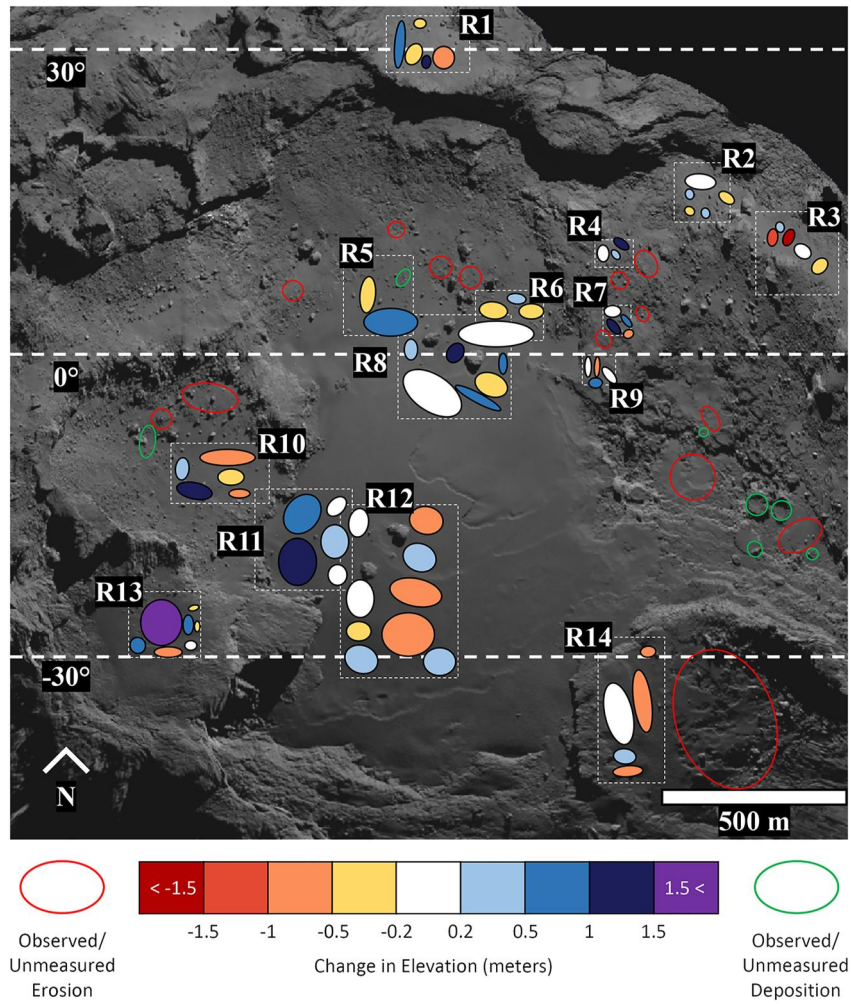

Figure 4. Sediment redistribution map for the smooth terrains in the Imhotep region and its immediate vicinity. Measurements for erosion and deposition were obtained for regions R1–R14 and are represented as shaded ellipses, where the colors of the ellipses correspond to the amount of erosion/deposition as per the legend. The maximum amount of deposition was observed in region R13 (Figure S20 in Supporting Information S1) at ∼30° S, while the maximum erosion was observed in region R3 (Figure S10 in Supporting Information S1) at ∼10° N. Regions where we observed clear evidence of erosion and deposition but were unable to produce digital elevation models have been indicated by transparent ellipses; more details can be found in Figures S1–S7 of the Supporting Information S1.

A potential criticism of our methodology is that the shape-from-shading algorithm obtains only slope (hence relative elevation) information from the images. Information about absolute elevations comes from the starting DEM. Because we start with the same global shape model for both time periods, the differences we calculate will measure variations in erosion and deposition within each region, but net changes across whole DEMs might not be reflected. In practice, we find that the net change values are accurate. From the images, we were able to identify subareas in which the distribution of small boulders (∼ meter scale) did not change in five of the 14 DEM regions. The estimated change in sediment elevation near such subareas is 0.09 ± 0.03 m (see Table S17 in Supporting Information S1 for details). Thus, we can draw reliable conclusions about net erosion or accumulation in different regions. It is likely that our selection of regions containing unchanging areas (needed to control the images) "anchors" the absolute elevations well enough to make such conclusions possible.

3. Results

To measure the re-distribution of sediment that occurred during 67P's perihelion passage, we investigated 14 ROIs within 67P's large lobe (Figures 1 and 4) following the process described in Section 2. Since the highest

21699100, 2024, 2, Downloaded from https://agupubs.onlinelibrary.wiley.com/doi/10.1029/2023JE008089 by Universite Cote D'azur, Wiley Online Library on [09/01/2025]. See the Terms and Conditions (https://onlinelibrary.wiley.com/terms-and-conditions) on Wiley Online Library for rules of use; OA articles are governed by the applicable Creative Commons License

21699100, 2024, 2, Downloaded from https://agupubs.onlinelibrary.wiley.com/doi/10.1029/2023JE008089 by Universite Cote D'azur, Wiley Online Library on [09/01/2025]. See the Terms and Conditions (https://onlinelibrary.wiley.com/terms-and-conditions) on Wiley Online Library for rules of use; OA articles are governed by the applicable Creative Commons License

insolation rates in Imhotep are at its southernmost latitudes, we expected more erosion in the south and more deposition in the north. We hypothesized that Imhotep would follow the global trends of south-to-north transport predicted by Keller et al. (2017), given its extensive coverage of latitudes on both sides of the equator. Surprisingly, we instead often observed hyper-localized differences in net erosion/accumulation of sediment (Figure 4), and broader east–west erosion–deposition trend across all of Imhotep. The largest deposition thicknesses we measured are at ∼30° S in region R13 on the western margin of Imhotep, while the largest erosion depths we measured are at ∼10° N in region R3 (Figure 4) on the eastern margin of Imhotep. Additionally, the significant differences in the total volumes of sediment eroded and/or deposited within regions that are separated by only tens of meters imply that local processes play a crucial role in the overall re-distribution of material. It is important to note that we only focus on the smooth terrains and do not look at the cliffs and more consolidated terrains, which do in fact appear more eroded in the south relative to the north (Vincent et al., 2017).

We observed significant erosion in the form of scarp-bounded pits (hereafter "scarps") that migrated through the smooth terrains throughout the perihelion (Jindal et al., 2022), often exposing underlying boulders. In region R12 (Figure 5a), we mostly observed deposition, except in sub-regions that were eroded by scarps following the large-scale deposition that occurred prior to perihelion (scarps "g," "h," "j" in Jindal et al., 2022). Although this region may have received a uniform airfall deposition, late-stage scarp-driven erosion resulted in the net accumulation of material in some sub-regions and the net loss of material in others (See Figure S19 in Supporting Information S1). We observed similar patterns in other parts of Imhotep, specifically regions R8 and R10, where areas that experienced scarp migration after perihelion exhibited a net loss of sediment even though regions in their immediate vicinity-accreted sediment. This is consistent with previous work (Jindal et al., 2022) and suggests that the most significant deposition of airfalling sediment within Imhotep occurred prior to perihelion, with post-perihelion scarp-driven erosion negating any deposition in very localized regions. Migrating scarps are also observed in Region U4 (Figures S1 and S5 in Supporting Information S1).

Region R13 (Figures 5g–5i) mostly accumulates material; the amount of accumulation, however, varies significantly within the regions. Specifically, we find that the topographic low that exists prior to the onset of activity in this region accumulates, on average, ∼2 m of material. Meanwhile, the higher lying topography that surrounds these initial low accumulates, on average, ∼0.5−1 m of material and at the same time also displays the erosion of material (Figure S20 in Supporting Information S1). This suggests that airfalling material must be mobilized after it is initially deposited on the surface, as airfall accumulation should be uniformly thick. We observe a similar increasing gradient of sediment accumulation in the downhill direction in region R7 (Figures 5a–5c) until the sediment is obstructed by boulders. Erosion further uphill (Figure S3 in Supporting Information S1) suggests that material may, like in region R13, be mobilized downslope over very local scales. Similar evidence of local down slope motion is observed in region R5, where the sediment appears to be moving down a relatively steep gravitational slope and accumulating in the gravitationally flat region.

The dune-like crests (hereafter "crests") that are found within many smooth deposits on 67P (Barrington et al., 2023; Jia et al., 2017; N. Thomas et al., 2015) were also frequently observed to move back-and-forth in a random pattern. Such crests do not appear to move in any preferred direction but instead migrate locally while staying broadly within their original locations. In regions R1 and R14, we measure local variations in deposition and erosion associated with such crests, variations we suppose are tied to this local movement.

Finally, we also observed new boulders exposed within talus deposits (Figures S2–S7 in Supporting Information S1) along the margins of smooth terrain deposits. We hypothesize that these boulder exposures result from downslope mass-wasting processes within the talus deposits. Depressions within region U6 (Figure S7 in Supporting Information S1), east of region R14 also expand radially, exposing underlying consolidated terrains. A significant amount of erosion is also measured in region U5 (Figure S6 in Supporting Information S1), where the nucleus below a small smooth terrain deposit is fully exposed. Interestingly, we also observed simultaneous deposition of significant quantities of sediment in the pre-existing circular features in the immediate vicinity of this patch undergoing erosion, which may be evidence of short-range transport of sediment. Previous studies estimated an erosion depth of ∼3.9 m (El-Maarry et al., 2017) based on the height of an exposed boulder, more than any other region for which we made measurements. Unfortunately, we are unable to make DEMs in both these regions as the underlying consolidated terrains and large boulders in the talus deposits comprise a significant portion of the surface. Instead, we denote their activity as transparent circles in Figure 4 (More Details can be found in Figures S1–S7 of the Supporting Information S1).

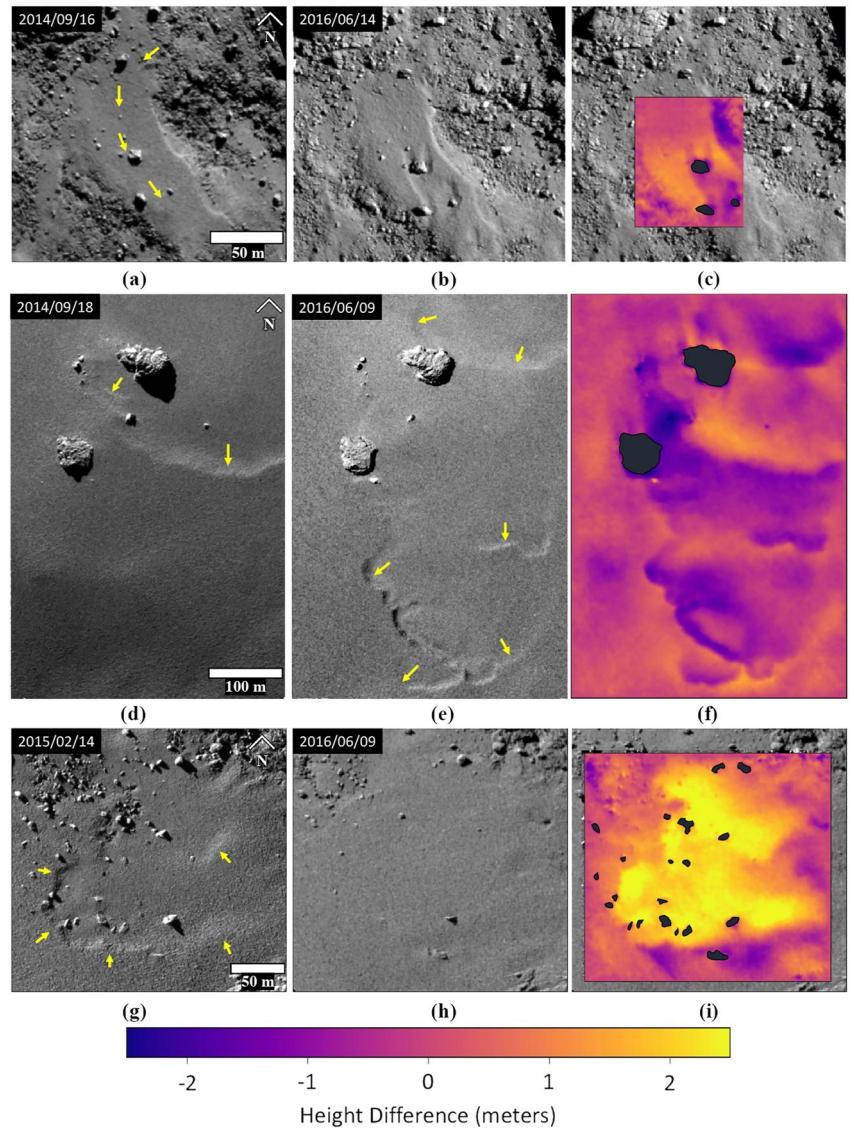

Figure 5. Influence of local-scale processes on sediment re-distribution. (a, b) Region R7 and its immediate surroundings in Periods 1 and 2, respectively. The yellow arrows indicate the gravitational downslope directions as interpreted from A.-T. Auger et al. (2015). (c) Sediment redistribution within R7. We see a gradient of material accumulation in the downslope direction until it is obstructed by the boulders. (d, e) Region R12 in Periods 1 and 2, respectively; the yellow arrows indicate scarps. (f) Sediment redistribution within R12, while most of the region-accumulated material, areas that experienced scarp migration display net erosion. (g, h) Region R13 and its immediate surroundings in Periods 1 and 2, respectively. The yellow arrows indicate the boundary of the initial topographic low in Period 1. (i) Sediment redistribution in R13, where the initial topographic low accumulates the most material. Large boulders are masked out in panels (c, f, i) because digital elevation models are not reliable in these areas.

4. Discussion

We provide the first comprehensive measurements for sediment transport across a large region of 67P—the Imhotep region and its immediate surroundings on the large lobe. We rely on the shape-from-shading technique to generate DEMs, which allows us to measure variations in topography at the pixel scale over large spatial areas. Previous research has investigated the topographic evolution of smooth terrains by measuring the shadow lengths for large, stationary boulders within these terrains (P. Cambianica et al., 2020, 2021); however, this technique only provides a height estimate in the immediate vicinity of the boulders. Our results are consistent to within error with the shadow length estimates of Cambianica et al. (2021) over the specific boulders of interest (highlighted in Figure S1 in Supporting Information S1) within region R8. Our work, however, allows for a more

21699100, 2024, 2, Downloaded from https://agupubs.onlinelibrary.wiley.com/doi/10.1029/2023JE008089 by Universite Cote D'azur, Wiley Online Library on [09/01/2025]. See the Terms and Conditions (https://onlinelibrary.wiley.com/terms-and-conditions) on Wiley Online Library for rules of use; OA articles are governed by the applicable Creative Commons License

21699100, 2024, 2, Downloaded from https://agupubs.onlinelibrary.wiley.com/doi/10.1029/2023JE008089 by Universite Cote D'azur, Wiley Online Library on [09/01/2025]. See the Terms and Conditions (https://onlinelibrary.wiley.com/terms-and-conditions) on Wiley Online Library for rules of use; OA articles are governed by the applicable Creative Commons License

complete investigation of the complex redistribution of sediment across the entire region and shows that the changes in the heights of the smooth terrain deposits are variable even on small spatial scales.

Our observations and measurements within the central basin of Imhotep (i.e., basin D as described in A.-T. Auger et al., 2015) suggests that it is experiencing net accumulation of material. The only material lost from the region directly correlates to locations where known scarps continued to erode the smooth terrains after the deposition that occurred during perihelion (Jindal et al., 2022). This is in contrast to the smooth terrains within the Hapi region in 67P's "neck" (El-Maarry et al., 2015). Despite being in a gravitational low (Keller et al., 2017) and experiencing polar winter for much of 67P's perihelion passage (Keller et al., 2015), Hapi appears to have only experienced net erosion (Birch et al., 2019). Scarps similar to the ones observed in the Imhotep region migrated through the region in the months prior to perihelion, exposing boulders in the process. Unlike in Imhotep, however, the boulders were never buried under sediment when the region was illuminated again post-perihelion. This goes against the expectation that smooth terrains are sinks for sediment. This difference between Imhotep and Hapi could indicate a difference in when the smooth terrains accumulated. In Hapi, material might accumulate in its smooth terrains under a different orbital configuration (L. Maquet, 2015) and/or through mass-wasting of material from the large bounding cliffs when the comet cools at aphelion (Haack et al., 2020). Meanwhile, Imhotep appears to experience net accumulation during perihelion due to its closer proximity to the more active consolidated terrains further south, which continuously deliver new sediment. Additionally, we observed signs of a dichotomy in the erosion and deposition of sediment between the eastern and western portions of Imhotep. The eastern portions of the basin seem to be mostly losing material, while the western half seems to mostly accrete material. We hypothesize that this may result from the rotation of 67P, where the western portion of the large lobe sweeps up particles lofted from the eastern half. That material was not observed to eject from Imhotep as easily as other regions (O. Groussin et al., 2015), lends support to this hypothesis, which could be investigated more thoroughly in follow-up studies.

We also observe that sediment re-distribution occurs on very local spatial scales, indicating that sediment transport pathways can be very short despite the very low gravity on 67P. We observe processes such as mass wasting, scarp migration, and crest motions, all of which have been extensively detailed in previous studies of 67P extensively. We also observe sediment motion down gentle slopes within smooth terrains that preferentially fill topographic lows (Figure 5). Our work provides an important first step toward quantifying the volume of material that falls back on to 67P's surface as airfall during its perihelion passage; previous works (Davidsson et al., 2021; Marschall et al., 2020) have attempted to estimate this fallback volume using dynamical models. By expanding our work to global scales, we can therefore more thoroughly separate global from local sediment transport processes. This would aid in understanding the context of any acquired sample for sample return missions such as the Comet Astrobiology Exploration SAmple Return (CAESAR, Squyres et al., 2018) that seek to target the smooth terrains for sample collection.

Acknowledgments
This research was supported by the Rosetta Data Analysis Program (80NSSC19K1307) and the Heising-Simons Foundation (51 Pegasi b Fellowship to S.P.D.B). We also express our gratitude to Oleg Alexandrov for supporting us with the Ames Stereo Pipeline. This research has made use of the scientific software shapeViewer (www.comet-toolbox.com). Proofreading was aided by OpenAI's ChatGPT tool. All OSIRIS image data presented in this paper were downloaded and are freely available on ESA's Planetary Science Archive (https://archives.esac.esa.int/psa) and NASA's Planetary Science Data System (https://pds.nasa.gov). Topographic data that support the plots within this paper and other findings of this study are available in the appendices and on Cornell University's eCommons (Jindal et al., 2023). Any use of trade, firm, or product names is for descriptive purposes only and does not imply endorsement by the U.S. Government. Finally, we thank the two anonymous reviewers and editors for providing valuable inputs that improved the manuscript.

Data Availability Statement

All images used in this study are available on ESA's Archive Image Browser and are credited to ESA/Rosetta/MPS for OSIRIS Team MPS/UPD/LAM/IAA/SSO/INTA/UPM/DASP/IDA—CC BY-SA 4.0 (https://image-archives.esac.esa.int) under the CC BY-SA 4.0 license. This license text can be found at https://creativecommons.org/licenses/by-sa/4.0/legalcode. This work also made use of the Integrated System for Imagers and Spectrometers (ISIS, https://isis.astrogeology.usgs.gov/) and the Ames Stereo Pipeline (https://stereopipeline.readthedocs.io/). Finally, all relevant Digital Elevation Models used in this study are available on Cornell University's eCommons (Jindal et al., 2023).

References

Acton, C. H. (1996). Ancillary data services of NASA's navigation and ancillary information facility. *Planetary and Space Science*, *44*(1), 65–70. https://doi.org/10.1016/0032-0633(95)00107-7

Agarwal, S., & Mierle, K. (2012). Ceres solver: Tutorial & reference. *Google Inc*, *2*(72), 8.

Alexandrov, O., & Beyer, R. A. (2018). Multiview shape-from-shading for planetary images. *Earth and Space Science*, *5*(10), 652–666. https://doi.org/10.1029/2018EA000390

Auger, A.-T., Groussin, O., Jorda, L., Bouley, S., Gaskell, R., Lamy, P. L., et al. (2015). Geomorphology of the Imhotep region on comet 67P/Churyumov-Gerasimenko from OSIRIS observations. *Astronomy & Astrophysics*, *583*, A35. https://doi.org/10.1051/0004-6361/201525947

Barrington, M. N., Birch, S. P. D., Jindal, A., Hayes, A. G., Corlies, P., & Vincent, J.-B. (2023). Quantifying morphological changes and sediment transport pathways on comet 67P/Churyumov-Gerasimenko. *Journal of Geophysical Research: Planets*, *128*(7), e2022JE007723. https://doi.org/10.1029/2022JE007723

Beyer, R. A., Alexandrov, O., & McMichael, S. (2018). The Ames Stereo Pipeline: NASA's open source software for deriving and processing terrain data. *Earth and Space Science*, *5*(9), 537–548. https://doi.org/10.1029/2018EA000409

Birch, S. P. D., Hayes, A. G., Umurhan, O. M., Tang, Y., Vincent, J.-B., Oklay, N., et al. (2019). Migrating scarps as a significant driver for cometary surface evolution. *Geophysical Research Letters*, *46*(22), 12794–12804. https://doi.org/10.1029/2019GL083982

Birch, S. P. D., Tang, Y., Hayes, A. G., Kirk, R. L., Bodewits, D., Campins, H., et al. (2017). Geomorphology of comet 67P/Churyumov–Gerasimenko. *Monthly Notices of the Royal Astronomical Society*, *469*(Suppl 2), S50–S67. https://doi.org/10.1093/mnras/stx1096

Cambianica, P., Cremonese, G., Fulle, M., Simioni, E., Naletto, G., Pajola, M., et al. (2021). Long-term measurements of the erosion and accretion of dust deposits on comet 67P/Churyumov–Gerasimenko with the OSIRIS instrument. *Monthly Notices of the Royal Astronomical Society*, *504*(2), 2895–2910. https://doi.org/10.1093/mnras/stab950

Cambianica, P., Fulle, M., Cremonese, G., Simioni, E., Naletto, G., Massironi, M., et al. (2020). Time evolution of dust deposits in the Hapi region of comet 67P/Churyumov-Gerasimenko. *Astronomy & Astrophysics*, *636*, A91. https://doi.org/10.1051/0004-6361/202037485

Davidsson, B. J., Birch, S., Blake, G. A., Bodewits, D., Dworkin, J. P., Glavin, D. P., et al. (2021). Airfall on comet 67P/Churyumov–Gerasimenko. *Icarus*, *354*, 114004. https://doi.org/10.1016/j.icarus.2020.114004

El-Maarry, M. R., Groussin, O., Thomas, N., Pajola, M., Auger, A.-T., Davidsson, B., et al. (2017). Surface changes on comet 67P/Churyumov-Gerasimenko suggest a more active past. *Science*, *355*(6332), 1392–1395. https://doi.org/10.1126/science.aak9384

El-Maarry, M. R., Thomas, N., Giacomini, L., Massironi, M., Pajola, M., Marschall, R., et al. (2015). Regional surface morphology of comet 67P/Churyumov-Gerasimenko from Rosetta/OSIRIS images. *Astronomy & Astrophysics*, *583*, A26. https://doi.org/10.1051/0004-6361/201525723

El-Maarry, M. R., Thomas, N., Gracia-Berná, A., Pajola, M., Lee, J.-C., Massironi, M., et al. (2016). Regional surface morphology of comet 67P/Churyumov-Gerasimenko from Rosetta/Osiris images: The southern hemisphere. *Astronomy & Astrophysics*, *593*, A110. https://doi.org/10.1051/0004-6361/201628634

Fornasier, S., Feller, C., Lee, J.-C., Ferrari, S., Massironi, M., Hasselmann, P. H., et al. (2017). The highly active Anhur–Bes regions in the 67P/Churyumov–Gerasimenko comet: Results from OSIRIS/*ROSETTA* observations. *Monthly Notices of the Royal Astronomical Society*, *469*(Suppl 2), S93–S107. https://doi.org/10.1093/mnras/stx1275

Fornasier, S., Hasselmann, P. H., Barucci, M. A., Feller, C., Besse, S., Leyrat, C., et al. (2015). Spectrophotometric properties of the nucleus of comet 67P/Churyumov-Gerasimenko from the OSIRIS instrument onboard the ROSETTA spacecraft. *Astronomy & Astrophysics*, *583*, A30. https://doi.org/10.1051/0004-6361/201525901

Groussin, O., Sierks, H., Barbieri, C., Lamy, P., Rodrigo, R., Koschny, D., et al. (2015). Temporal morphological changes in the Imhotep region of comet 67P/Churyumov-Gerasimenko. *Astronomy & Astrophysics*, *583*, A36. https://doi.org/10.1051/0004-6361/201527020

Haack, D., Otto, K., Gundlach, B., Kreuzig, C., Bischoff, D., Kührt, E., & Blum, J. (2020). Tensile strength of dust-ice mixtures and their relevance as cometary analog material. *Astronomy & Astrophysics*, *642*, A218. https://doi.org/10.1051/0004-6361/202037763

Hapke, B. (2012). *Theory of reflectance and emittance spectroscopy* (2nd ed.). Cambridge University Press. https://doi.org/10.1017/CBO9781139025683

Hu, X., Shi, X., Sierks, H., Fulle, M., Blum, J., Keller, H. U., et al. (2017). Seasonal erosion and restoration of the dust cover on comet 67P/Churyumov-Gerasimenko as observed by Osiris onboard Rosetta. *Astronomy & Astrophysics*, *604*, A114. https://doi.org/10.1051/0004-6361/201629910

Jia, P., Andreotti, B., & Claudin, P. (2017). Giant ripples on comet 67P/Churyumov–Gerasimenko sculpted by sunset thermal wind. *Proceedings of the National Academy of Sciences*, *114*(10), 2509–2514. https://doi.org/10.1073/pnas.1612176114

Jindal, A., Birch, S., Hayes, A., Özyurt, F. P., Issah, A., Barrington, M., et al. (2023). *Digital elevation model data from: Measuring erosional and depositional patterns across comet 67P's Imhotep region*. Cornell University eCommons Repository. https://doi.org/10.7298/qgyq-ym43

Jindal, A. S., Birch, S. P. D., Hayes, A. G., Umurhan, O. M., Marschall, R., Soderblom, J. M., et al. (2022). Topographically influenced evolution of large-scale changes in comet 67P/Churyumov-Gerasimenko's imhotep region. *The Planetary Science Journal*, *3*(8), 193. https://doi.org/10.3847/PSJ/ac7e48

Keller, H. U., Barbieri, C., Lamy, P., Rickman, H., Rodrigo, R., Wenzel, K. P., et al. (2007). OSIRIS – The scientific camera system onboard Rosetta. *OSIRIS The Scientific Camera System Onboard Rosetta*, *128*(1–4), 433–506. https://doi.org/10.1007/s11214-006-9128-4

Keller, H. U., Mottola, S., Davidsson, B., Schröder, S. E., Skorov, Y., Kührt, E., et al. (2015). Insolation, erosion, and morphology of comet 67P. *Churyumov-Gerasimenko*, *583*, A34. https://doi.org/10.1051/0004-6361/201525964

Keller, H. U., Mottola, S., Hviid, S. F., Agarwal, J., Kührt, E., Skorov, Y., et al. (2017). Seasonal mass transfer on the nucleus of comet 67P/Chuyumov–Gerasimenko. *Monthly Notices of the Royal Astronomical Society*, *469*(Suppl_2), S357–S371. https://doi.org/10.1093/mnras/stx1726

Kirk, R., Barrett, J., & Soderblom, L. (2003). Photoclinometry made simple…? In *Advances in Planetary Mapping 2003*. Retrieved from https://astropedia.astrogeology.usgs.gov/download/Research/ISPRS/Kirk_isprs_mar03.pdf

Lesage, E., Schmidt, F., Andrieu, F., & Massol, H. (2021). Constraints on effusive cryovolcanic eruptions on Europa using topography obtained from Galileo images. *Icarus*, *361*, 114373. https://doi.org/10.1016/j.icarus.2021.114373

Levison, H. F., & Duncan, M. J. (1997). From the Kuiper Belt to Jupiter-Family comets. *The Spatial Distribution of Ecliptic Comets*, *127*(1), 13–32. https://doi.org/10.1006/icar.1996.5637

Lohse, V., Heipke, C., & Kirk, R. L. (2006). Derivation of planetary topography using multi-image shape-from-shading. *Planetary and Space Science*, *54*(7), 661–674. https://doi.org/10.1016/j.pss.2006.03.002

Maquet, L. (2015). The recent dynamical history of comet 67P/Churyumov-Gerasimenko. *Astronomy & Astrophysics*, *579*, A78. https://doi.org/10.1051/0004-6361/201425461

Marschall, R., Markkanen, J., Gerig, S.-B., Pinzón-Rodríguez, O., Thomas, N., & Wu, J.-S. (2020). The dust-to-gas ratio, size distribution, and dust fall-back fraction of comet 67P/Churyumov-Gerasimenko: Inferences from linking the optical and dynamical properties of the inner comae. *Frontiers in Physics*, *8*, 227. https://doi.org/10.3389/fphy.2020.00227

Pajola, M., Höfner, S., Vincent, J. B., Oklay, N., Scholten, F., Preusker, F., et al. (2017). The pristine interior of comet 67P revealed by the combined Aswan outburst and cliff collapse. *Nature Astronomy*, *1*(5), 0092. https://doi.org/10.1038/s41550-017-0092

Preusker, F., Scholten, F., Matz, K.-D., Roatsch, T., Willner, K., Hviid, S. F., et al. (2015). Shape model, reference system definition, and cartographic mapping standards for comet 67P/Churyumov-Gerasimenko - Stereo-photogrammetric analysis of Rosetta/Osiris image data. *Astronomy & Astrophysics*, *583*, A33. https://doi.org/10.1051/0004-6361/201526349

Squyres, S. W., Nakamura-Messenger, K., Mitchell, D. F., Moran, V. E., Houghton, M. B., Glavin, D. P., & Caesar Project Team. (2018). The CAESAR new frontiers mission: 1. Overview. In *49th annual Lunar and planetary science conference* (p. 1332).

Tang, Y., Birch, S. P. D., Hayes, A. G., Kirk, R., Kutsop, N., Vincent, J. B., & Squyres, S. (2019). Generation of photoclinometric DTMs for application to transient changes on the surface of comet 67P/Churyumov-Gerasimenko. *Astronomy & Astrophysics*, *630*, A10. https://doi.org/10.1051/0004-6361/201834127

21699100, 2024, 2, Downloaded from https://agupubs.onlinelibrary.wiley.com/doi/10.1029/2023JE008089 by Universite Cote D'azur, Wiley Online Library on [09/01/2025]. See the Terms and Conditions (https://onlinelibrary.wiley.com/terms-and-conditions) on Wiley Online Library for rules of use; OA articles are governed by the applicable Creative Commons License

Tenthoff, M., Wohlfarth, K., & Wöhler, C. (2020). High resolution digital terrain models of mercury. *Remote Sensing*, *12*(23), 3989. https://doi.org/10.3390/rs12233989

Thomas, N., Davidsson, B., El-Maarry, M. R., Fornasier, S., Giacomini, L., Gracia-Berná, A. G., et al. (2015). Redistribution of particles across the nucleus of comet 67P/Churyumov-Gerasimenko. *Astronomy & Astrophysics*, *583*, A17. https://doi.org/10.1051/0004-6361/201526049

Thomas, N., El Maarry, M., Theologou, P., Preusker, F., Scholten, F., Jorda, L., et al. (2018). Regional unit definition for the nucleus of comet 67P/Churyumov-Gerasimenko on the SHAP7 model. *Planetary and Space Science*, *164*, 19–36. https://doi.org/10.1016/j.pss.2018.05.019

van Diggelen, J. (1951). A photometric investigation of the slopes and the heights of the ranges of hills in the Maria of the Moon. *Bulletin of the Astronomical Institutes of the Netherlands*, *11*, 283–289.

Vincent, J.-B., Hviid, S. F., Mottola, S., Kuehrt, E., Preusker, F., Scholten, F., et al. (2017). Constraints on cometary surface evolution derived from a statistical analysis of 67P's topography. *Monthly Notices of the Royal Astronomical Society*, *469*(Suppl 2), S329–S338. https://doi.org/10.1093/mnras/stx1691

21699100, 2024, 2, Downloaded from https://agupubs.onlinelibrary.wiley.com/doi/10.1029/2023JE008089 by Universite Cote D'azur, Wiley Online Library on [09/01/2025]. See the Terms and Conditions (https://onlinelibrary.wiley.com/terms-and-conditions) on Wiley Online Library for rules of use; OA articles are governed by the applicable Creative Commons License